nature catalysis

Article

https://doi.org/10.1038/s41929-026-01593-w

Bimodal multiphoton catalysis via structural regeneration

Received: 9 September 2025

Accepted: 7 July 2026

Published online: 14 August 2026

Check for updates

Cristian Rosso[1,5], Giorgia Barison[1,5], Federico Droghetti[2], Nicola Michelazzo[1], Andrea Sartorel[1], Giorgio Pelosi[3], Marco Bortolus[1], Sara Bonacchi[1], Stefano Visentini[1], Alessia Marrese[1], Giovanni Bistoni[4], Sofia Lerda[4], Vittoria Burigana[1], Elisabetta Collini[1], Paolo Costa[1], Mirco Natali[2] & Luca Dell'Amico[1]

Most of the current photocatalytic methodologies for the generation of reactive radical intermediates have limited redox windows and can operate within a single redox manifold. Here, to overcome these constraints, we report a purely organic photocatalyst that operates via a two-photon excitation mechanism, enabling both oxidative and reductive transformations within a unified platform. Upon visible-light irradiation, the molecule undergoes reversible fragmentation into three reactive subunits spanning a 5.7 V redox window. These fragments orchestrate an unusual consecutive light-induced electron-transfer mechanism that enables the orthogonal activation of thermodynamically challenging substrates. The mechanistic scenario is revealed through a combination of spectroscopic and optical techniques, supported by quantum calculations. Selectivity is mainly governed by the activity of a transiently generated catalytic species, whose presence prevents the need for external radical-sorting agents. Finally, the generality of this light-driven radical-coupling reactivity is demonstrated across a broad range of structurally diverse substrates.

The use of visible-light photocatalysis to promote chemical transformations has redefined synthetic chemistry, providing access to reactive intermediates under mild conditions[1–3]. Light energy can trigger substrate activation through a variety of mechanistic pathways, including energy transfer, atom transfer or electron transfer[4–6]. Among these, electron transfer, commonly referred to as photoredox catalysis, has become a major strategy, operating via either oxidative or reductive quenching events. Central to this approach is the ability of photocatalysts (PCs) to engage in single-electron transfer (SET) processes, allowing for the generation of radical species from substrates that would otherwise remain inert under thermal or ground-state conditions. However, the inherent energy limitations of one-photon excitation, combined with the relatively narrow redox potential windows accessible by most PCs, restrict the scope of accessible reactivity[1,4,7–9]. Overcoming these constraints requires a departure from classical paradigms. An ideal approach involves the design of photocatalytic systems that operate across multiple redox manifolds, enabling both oxidative and reductive transformations within a unified platform. Such bimodal PCs challenge the conventional dichotomy of redox reactivity, functioning as both photo-oxidants and photoreductants depending on their structural nature, as well as the nature of the starting substrates and reaction conditions. However, under one-photon catalytic manifolds, a single PC can operate only in either a reductive or an oxidative quenching regime (Fig. 1a,b)[10–12].

In parallel, proton-coupled electron-transfer[13–15], electrophotochemical approaches or multiphoton excitation[9,16] is redefining

[1]Department of Chemical Sciences, University of Padova, Padova, Italy. [2]Department of Chemical, Pharmaceutical and Agricultural Sciences, University of Ferrara, Ferrara, Italy. [3]Department of Chemistry, Life Sciences and Environmental Sustainability, University of Parma, Parma, Italy. [4]Department of Chemistry, Biology and Biotechnology, University of Perugia, Perugia, Italy. [5]These authors contributed equally: Cristian Rosso, Giorgia Barison. e-mail: luca.dellamico@unipd.it

https://doi.org/10.1038/s41929-026-01593-w

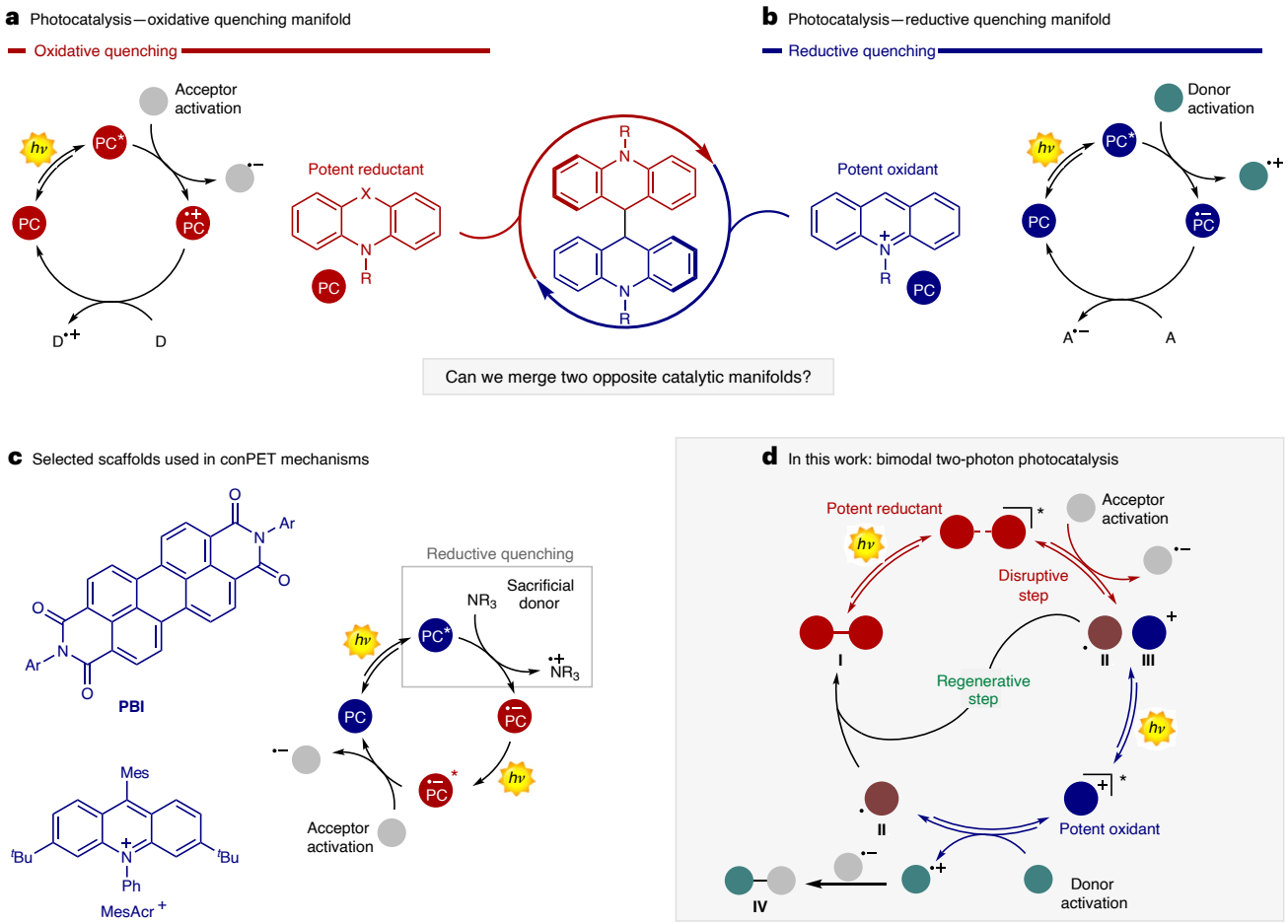

Fig. 1 | From conventional photocatalysis to dynamic photocatalysis. **a**, Conventional photocatalytic oxidative quenching manifold. **b**, Conventional photocatalytic reductive quenching manifold. **c**, Common scaffolds employed in conPET mechanisms. **d**, The unconventional reaction manifold for dynamic photocatalysis. PBI, perylene bisimide; $MesAcr^+$, 9-mesityl-3,6-di-*tert*-butyl-10-phenylacridinium; ^{t}Bu, *tert*-butyl; Ar, aryl; NR_3, tertiary amine; D, donor; A, acceptor.

what is thermodynamically possible under visible-light irradiation[17–19]. By harnessing the energy of sequential photons, it becomes feasible to access excited states or intermediates that show reactivity far beyond that achievable with single-photon processes, thus allowing the activation of redox-inert substrates. Under reported two-photon excitation mechanisms, the PC initially engages in a reductive quenching pathway. However, current processes typically rely on the use of sacrificial reductants that do not directly participate in product formation (Fig. 1c). Despite notable advances, the concurrent activation of opposite redox manifolds within a single reaction remains elusive, owing to limitations in catalyst stability and the tendency of reactive intermediates to self-quench[5]. Further complicating the development of such an unconventional process is the concomitant generation of diverse radical species, which can lead to randomized side products and/or the PC's deactivation.

In this Article, we introduce bimodal multiphoton catalysis, which transcends these limitations. Upon light activation, the PC undergoes controlled bond cleavage, generating distinct reactive intermediates that, upon a second photochemical stimulus, are capable of performing opposite redox processes: reduction and oxidation (Fig. 1d). These catalytic intermediates finally recombine to restore the original PC's structure, enabling cyclic and efficient two-photon bimodal catalysis.

We demonstrate the potential of dynamic photocatalysis using a purely organic dimeric PC (**I**), which operates under two-photon visible-light irradiation. Upon absorption of the first photon, the catalyst engages in the reduction of the first substrate and undergoes fragmentation, generating two distinct species (Fig. 1d): a radical intermediate (**II**; brown circle) and a cationic species (**III**; blue circle), each driving a separate reaction pathway. Absorbing a second photon, **III** acts as a potent photo-oxidant that oxidizes the second substrate (green circle) via a reductive quenching mechanism. This process regenerates another radical (**II**), which subsequently recombines, restoring the original dimeric PC (**I**). In contrast to classical consecutive photoinduced electron transfer (conPET) processes, the two activated substrates undergo coupling, yielding the final product (**IV**). This divergent redox approach enables the activation of substrates with opposing redox properties, effectively expanding the accessible redox window beyond conventional multiphoton excitation manifolds. We leverage this strategy to activate thermodynamically challenging bonds (C–Si, C–B, C–X and C–O) in a single step under very mild conditions. Moreover, we establish that this catalytic platform is general and can be readily extended to a broad range of functional groups and substrates, granting high selectivity without the need for any radical-sorting agent. By overcoming two fundamental limitations of organic photocatalysis, such as the limited redox window and inherent instability of the organic dyes, dynamic photocatalysis harnesses structural fragility as a functional advantage.

Results

Development of the photocatalytic platform and reaction optimization

We began trying to identify a catalytic system capable of overcoming the classical dichotomous view of oxidative versus reductive quenching

https://doi.org/10.1038/s41929-026-01593-w

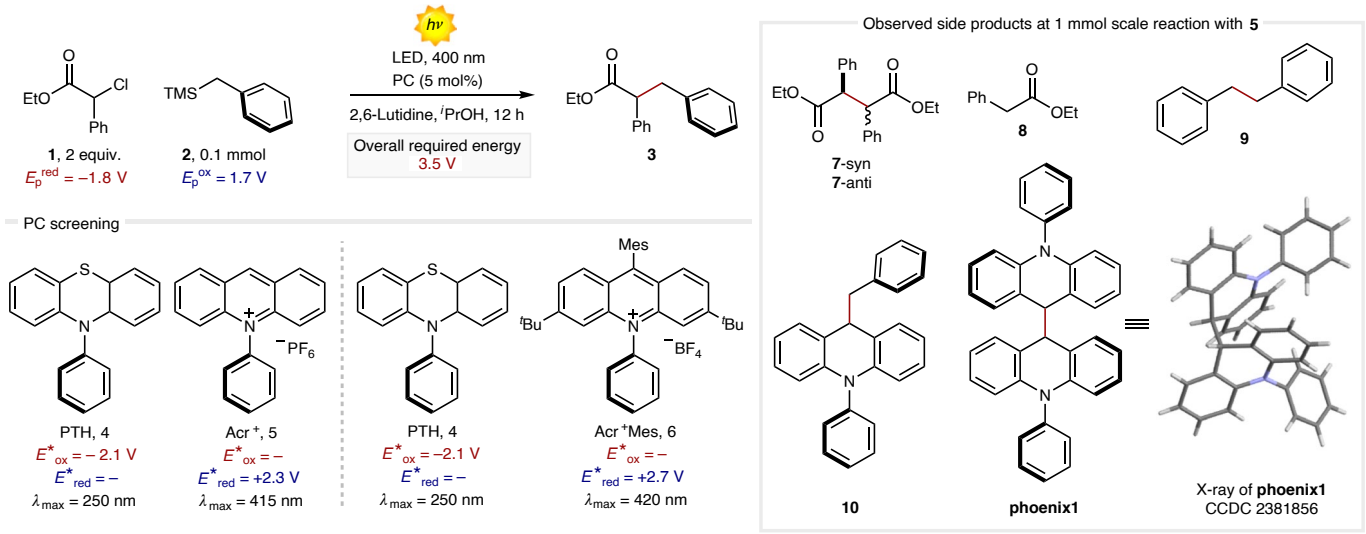

Fig. 2 | Development of the photocatalytic platform and reaction optimization. Reaction conditions: **1** (0.2 mmol), **2** (0.1 mmol), PC (5 mol%, unless otherwise noted), 2,6-lutidine (0.3 mmol) in *i*PrOH [0.1 M], irradiated with a 50-W Kessil lamp (400 nm, 3 cm distance) under a nitrogen atmosphere at 30 °C. The yields in parentheses refer to the average isolated products obtained from two independent reactions. PTH, 10-phenylphenothiazine; Acr+, 10-phenylacridinium hexafluorophosphate; Acr+Mes, 9-mesityl-3,6-di-*t*-butyl-10-phenylacridinium tetrafluoroborate; LED, light-emitting diodes. The asterisk denotes PC loading at 2.5 mol%.

processes[1,4,5]. We thus selected two alternative and thermodynamically opposed catalytic cycles in which the starting reagents, namely ethyl 2-chloro-2-phenylacetate (**1**) and benzyltrimethylsilane (**2**), are activated by either highly reducing (phenothiazine **4**) or highly oxidizing (acridinium ions **5** or **6**) PCs. After the two activation steps, ethyl 2,3-diphenylpropanoate (**3**) potentially forms upon radical combination (*vide infra*). The reduction of **1** shows an irreversible peak potential, E_p^{red}, below −1.8 V versus the saturated calomel electrode (SCE; Supplementary Fig. 24), which refers to a DET process controlled by a high activation barrier[20,21], whereas the oxidation of **2** requires more than +1.7 V versus the SCE (E_p^{ox}; Supplementary Fig. 11), as expected for a stepwise dissociation process. For such processes, the electrochemical peak potentials (E_p) do not directly correspond to standard redox potentials ($E°$), particularly in the case of DET reactions with a high activation barrier (see 'Electrochemical Characterization' in Supplementary Information). The overall energy window required for this process is as high as 3.5 V, seemingly precluding the use of visible light to promote this process.

We initially evaluated a series of single state-of-the-art PCs in the presence of 2,6-lutidine as base and 2-propanol (*i*PrOH) as solvent, but none led to any appreciable results (Supplementary Fig. 3). We thus started to mix structurally diverse PCs to evaluate the possibility of merging the two opposed quenching cycles, as we thought that the great difference between the redox potentials of the two PCs would have slowed down the cross-quenching process of the excited species in an inverted Marcus regime, while favouring the activation of the two substrates[22]. Many PC pairs were completely ineffective (Fig. 2 and Supplementary Table 1). However, the mixture of 10-phenyl-phenothiazine (**4**) and 10-phenylacridiumium hexafluorophosphate (**5**) gave intriguing results, furnishing product **3** in 16% yield (Fig. 2, entry 2). Surprisingly, replacing **5** with the more structurally stable derivative 9-mesityl-10-phenylacridinium tetrafluoroborate (**6**) completely inhibited the observed reactivity (entry 3). We thus used the different PCs individually to evaluate the performance of the different scaffolds (entries 4–6). Curiously, the sole compound **5** furnished the product in an encouraging 33% yield (entry 6). We then carefully analysed the crude reaction mixture, performing the transformation at 1 mmol scale to identify all the products and by-products, while aiming to recover the PC and the remaining starting materials. Intriguingly, apart from bibenzyl (**9**), deriving from the oxidative activation of the C–Si bond and subsequent homocoupling reaction, we found the diester (**7**) arising from reduction and homodimerization of the α-chloro reagent **1**. Similarly, we detected the corresponding dehalogenated ester (ethyl 2-phenylacetate, **8**) (Supplementary Table 1). We then wondered which species in solution was promoting the reduction of **1**. We found the answer by looking at the crude reaction mixture, from which we were able to identify, isolate and characterize the benzylated dihydroacridine (9-benzyl-10-phenyl-9,10-dihydroacridine, **10**) and the tetrahydrobiacridine (**phoenix1**). No trace of the original PC **5** was detected. To understand the impact of these new species in the process, we performed the reaction with **10** and **phoenix1** under catalytic conditions (5 mol% PC loading; Supplementary Table 1). The first species (entry 7) gave appreciable results leading to a 42% yield. However, the crude mixture at the end of the reaction showed the formation of **phoenix1** as the only photoactive species, while the original PC **10** was not detected. Notably, the reaction performed in the presence of **phoenix1** (entry 8) furnished product **3** in 53% yield (50% isolated), while showing the presence of the same PC at the end of the reaction. We thus assumed that, in the reactions catalysed by either **5** or **10**, the transformation proceeds via the in situ formation of the same key catalytic species, that is, the dimeric **phoenix1** (vide infra). Further optimization, including solvents, bases, stoichiometry and light (Supplementary Tables 2–9), allowed us to isolate product **3** in 56% yield using only 2.5 mol% catalyst loading (entry 9). No reaction was observed in the absence of **phoenix1** or light. Alternative PC variants were also evaluated, resulting in very similar yields (Supplementary Table 1).

Mechanistic insights from spectroscopic measurements

The initial discovery of an efficient photocatalytic platform raised two key questions: How can the single **phoenix1** activate both substrates **1** and **2** via opposed quenching cycles? How is **phoenix1** generated from **5** or **10** in the reaction media? To address these points and gain insight into the reaction manifold, we performed pump–probe measurements and laser flash photolysis (LFP) at femtosecond (fs) and nanosecond (ns) scales, respectively. Crucially, femtosecond transient absorption spectroscopy unambiguously established the photoionization[22] of **phoenix1** upon 400 nm excitation (Supplementary Equations (1)–(5)), producing a solvated electron and radical **11**. A diagnostic transient

absorption signal above 600 nm, characteristic of solvated electrons in *i*PrOH, was observed alongside the distinct signature of radical **11** (Fig. 3a, left)[23,24]. Interestingly, we were also able to define the kinetics of the excitation and electron release, corresponding to 150 fs and 230 fs, respectively (see 'Photophysical Studies' in Supplementary Information). Further experiments were performed at the ns scale. Light excitation of **phoenix1**, in the absence of substrate **1**, further corroborates the photoionization process. The transient spectrum measured at 10 ns (Fig. 3a, centre) is indeed characterized by two absorptions at 355 nm and 520 nm and a broad signal above 550 nm. The former can be attributed to the acridinyl radical **11** (Fig. 3)[24,25], whereas the latter can be assigned to residual solvated electrons in alcoholic solution[24], both generated following Supplementary Equations (1)–(3). Quantitative analysis of the respective concentrations (see 'Photophysical Studies' in Supplementary Information) indicates that the amount of acridinyl radical **11** is considerably larger than that of solvated electrons. This suggests that the present experiment is tracking the final step of a fast charge recombination between the photo-generated electrons and acridinium ion **5** (Supplementary Equation (4)), observed in the fs analysis. Consistent with this hypothesis, the absorption band at 520 nm characteristic of the acridinyl radical **11** slightly increases in the following 500 ns (Supplementary Fig. 58), while the absorption above 550 nm practically disappears. The subsequent spectral changes are monotonic and track the decay of the acridinyl radical **11** through radical recombination (Supplementary Equation (5)), leading to the regeneration of **phoenix1** (so named because of its unusual photochemical behaviour: upon light excitation, the molecule undergoes disruption and subsequent regeneration, analogous to the mythological rebirth of the phoenix). The decay of both absorptions at 355 nm and 520 nm indeed follows a well-behaved second-order kinetic trend (Supplementary Fig. 57) from which a bimolecular rate constant of $k = 1.1 \times 10^9\ M^{-1}\ s^{-1}$ can be extracted. To rule out the hypothesis of a classical oxidative quenching manifold, we also perform Stern–Volmer quenching experiments. However, no emission was observed from **phoenix1** excitation at diverse wavelengths, even when the experiments were conducted at 77 K. The photoionization process is extremely fast, as corroborated by fs LFP, and accounts for the missing emission. Even assuming the presence of an initially light-generated S_1 excited state, this will not have sufficient lifetime to drive any redox event. The generation of solvated electrons and radical **11** upon light irradiation of **phoenix1** was further confirmed by spin-trapping electron paramagnetic resonance (EPR) experiments, using 3,4-dihydro-2,3--dimethyl-2*H*-pyrrole-1-oxide (DMPO) as a spin trap (Fig. 3b and Supplementary Figs. 79–81). While no radicals were detected under dark conditions, irradiation at 355 nm quickly produced two trapped radicals coming from **phoenix1**: one ascribable to the trapping of the solvated electron (nine-line green simulation)[26] and one compatible with the trapping of **11** (six-line brown simulation). Simulation of the mixture of these two radicals (red lines) matches very well the recorded spectra (black line), in which the residual signal comes from the trapping of solvent radicals. Consistent with these findings, when the experiment is repeated in the presence of an electron scavenger, such as potassium nitrate[27], the nine-line spectrum is not observed (Supplementary Fig. 79). Along with those measurements, we performed a photochemical Birch reaction with anthracene to confirm **phoenix1**'s ability to generate solvated electrons (Supplementary Information, page 107). Accordingly, we performed the catalytic reaction in the presence of this scavenger, and we observed a significant drop in yield from 61% to 13%, indicating that the generation of free solvated electrons is a key step to drive the studied reactivity. We also performed cyclic voltammetry (CV) studies. Under an anodic scan, **phoenix1** shows an irreversible anodic wave with a peak potential at +0.4 V versus the SCE while a cathodic peak at −0.3 V versus the SCE appears during the backward scan (Supplementary Fig. 47). Importantly, the same reduction peak was not observed if a cathodic scan was performed as a forward scan, highlighting that the reductive process is related to the species that forms upon the oxidation of **phoenix1**.

Most importantly, consecutive anodic and cathodic traces (Supplementary Fig. 48) show that the original PC scaffold **phoenix1** can be efficiently regenerated. We found that **phoenix1** undergoes a two-electron oxidation at the anode, forming acridinium **5**, as confirmed by both CV and spectroelectrochemical analysis (SEC) of the isolated compound (Fig. 3c and Supplementary Fig. 50).

Reductive quenching manifold

In the presence of **1**, the transient spectrum measured for **phoenix1** at 10 ns (Fig. 3c, right) shows the lack of the absorption signal above 550 nm and the presence of an additional absorption centred at 420 nm, characteristic of acridinium ion **5**, pointing to the effective reaction between solvated electrons ($E = -3.3$ V/−3.5 V versus the SCE)[28–30] and **1**. Furthermore, the absorption signals at 355 nm and 420 nm remain persistent at longer times (Fig. 3a and Supplementary Fig. 58), supporting the accumulation of acridinium **5** in solution due to the irreversible nature of the reduction process. Once acridinium **5** forms, it can absorb visible light, enabling an oxidative reaction ($E^*_{red} = +2.3$ V versus the SCE for the singlet excited state). Interestingly, emission spectra show that the singlet excited state of **5** is efficiently quenched by substrate **2** through a dynamic process. Stern–Volmer analysis (Supplementary Fig. 75) yields a bimolecular rate constant of $k = 4.0 \times 10^9\ M^{-1}\ s^{-1}$ for this reaction. LFP analysis confirms the occurrence of an irreversible PET that leads to the formation of acridinyl radical **11** (positive absorption between 450 nm and 500 nm; Fig. 3a centre and Supplementary Fig. 77). The latter then decays via radical recombination with another radical **11** (or with the benzyl radical **13**, vide infra), thereby regenerating **phoenix1** and closing the catalytic cycle (see 'Photophysical Studies' in Supplementary Information). Interestingly, through CV and SEC analysis, we also proved that acridinium **5** can be reconverted into **phoenix1** by switching the applied potential from +0.5 V to −0.5 V via the formation and sequential recombination of radicals **11** (Fig. 3c and Supplementary Fig. 50)[31]. We further conducted a bulk electrolysis experiment, in which the reduction of acridinium **5** led to the formation of **phoenix1** in 17% isolated yield upon simple filtration (see 'Bulk Electrolysis' in Supplementary Information).

Dynamic photocatalysis

On the basis of these data and experimental results, we propose the dynamic catalytic cycle illustrated in Fig. 3e. **phoenix1** is excited by light and rapidly (<1 ns) undergoes photoionization to deliver radical **11**, the acridinium **5** and a free electron in solution. These solvated electrons are responsible for the reduction of **1**, having an $E = -3.3$ V/−3.5 V versus the SCE[28–30]. Upon reductive C–Cl bond cleavage, the reactive radical **12** is produced. Subsequently, **5** is photoexcited to its S_1 state ($E^*_{red} = +2.3$ V versus the SCE), which is promptly quenched by **2**, delivering the corresponding radical **11**. The oxidation of **2** leads to the loss of the trimethylsilyl group and the generation of benzyl radical **13**. The thus-formed open-shell species **12** and **13** lead to the coupling product **3**, while the two radicals **11** recombine to regenerate the parent **phoenix1**. It is worth noting that only aromatic derivatives **1** form radicals **12** with lifetimes sufficiently long to undergo coupling with the so-formed benzylic radical **13** in synthetically useful yields (Fig. 5). By contrast, α-chloro esters bearing an unstabilized CH_2 group afforded only trace amounts of the corresponding coupling products **3**. The catalytic cycle in Fig. 3e was supported by calculations carried out at the M062X/def2-TZVP-CPCM (*i*PrOH) level of theory (Supplementary Fig. 54). The investigation of the photoionization was carried out by considering a vertical transition of **phoenix1** into its first singlet excited state, S_1, and its subsequent relaxation to the minimum of the excited potential energy surface. In its relaxed geometry, the excited system was observed to spontaneously dissociate into two fragments, with the C–C previously connecting the two units reaching a value of about 3.14 Å. The TD-DFT calculations

https://doi.org/10.1038/s41929-026-01593-w

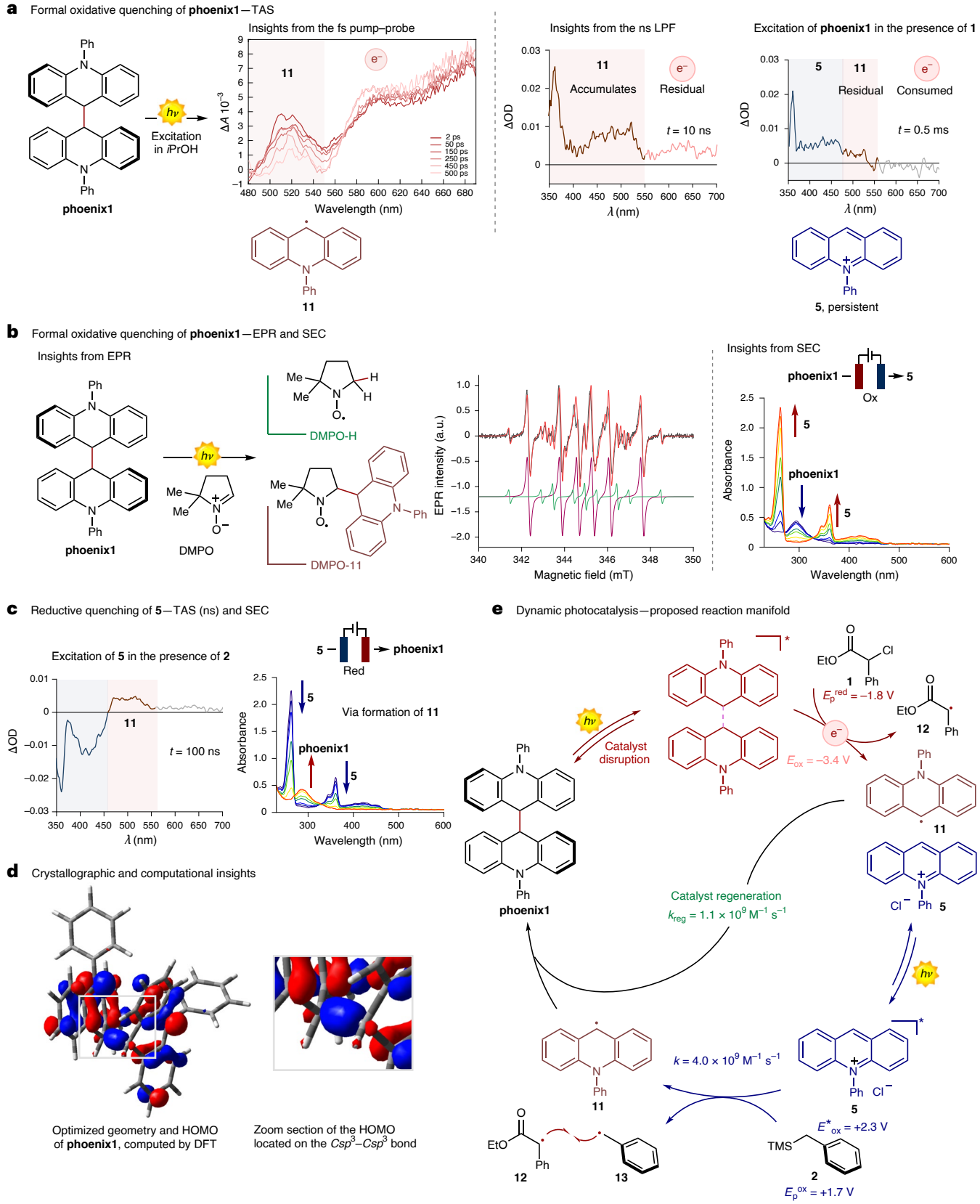

Fig. 3 | Mechanistic investigation. a, Femtosecond pump–probe and nanosecond LFP studies of transient photoexcited species. **b**, Spectra from EPR and SEC spectroscopies. **c**, SEC analysis supporting the reductive quenching pathway. **d**, Computational analysis at the (U)M06-2X/def2-TZVP level with IEFPCM (*i*PrOH), showing the energetics of the proposed intermediates and reaction steps. **e**, Proposed dynamic photocatalytic reaction manifold. Potentials are reported versus the SCE unless otherwise noted. DMPO, 3,4-dihydro-2,3-dimethyl-2*H*-pyrrole 1-oxide; TAS, transient absorption spectroscopy; OD, optical density.

https://doi.org/10.1038/s41929-026-01593-w

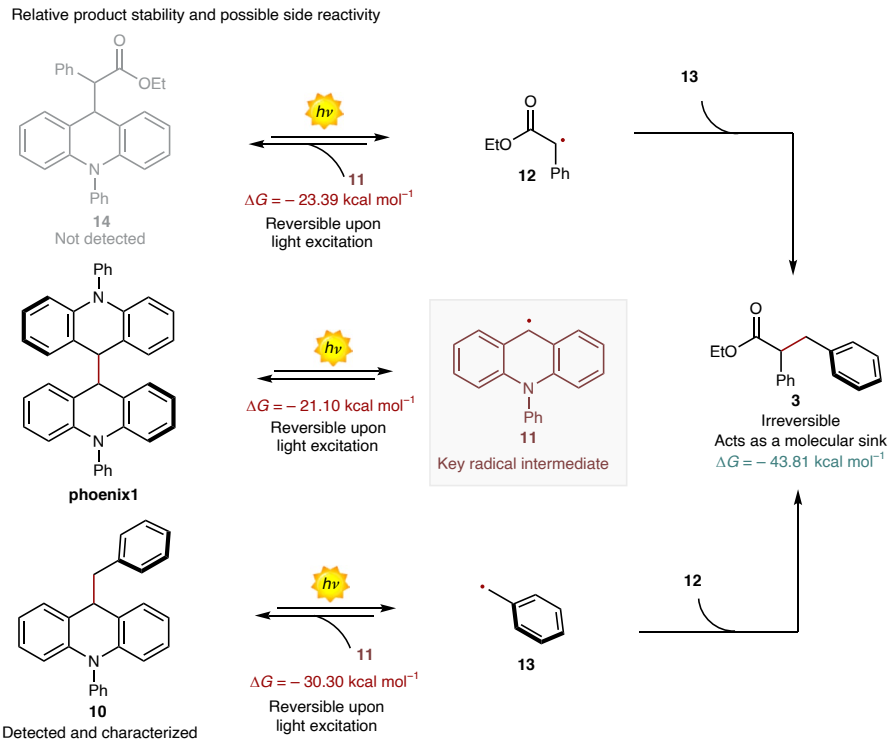

Fig. 4 | Collateral pathways for the proposed reaction manifold. Relative product stability and possible alternative PC reactivity.

indicated that the lowest energy absorption band is dominated by the electronic transition from the highest occupied molecular orbital to the lowest occupied molecular orbital, and thus is responsible for a reduction of the bonding character between the dihydroacridine units and corroborates the experimentally observed C–C dissociative excitation pathway in **phoenix1** (Supplementary Fig. 51).

Selectivity of the process and overall mechanistic picture

The proposed reaction mechanism involves the generation of several radical species that are produced at different rates (Fig. 3a and 'Computational Studies' in Supplementary Information), allowing the formation of product **3** and the regeneration of the catalyst. However, a randomized combination of these reactive species may lead to a complex and unproductive reaction outcome. We questioned how, in this puzzling situation, the reaction led to the formation of the desired product **3** in 61% NMR yield and to the virtually quantitative regeneration of the original catalyst **phoenix1**. To this end, we calculated the free energies of the possible coupling products originating from the key intermediate **11** (Fig. 4). This species is generated upon the initial light irradiation as well as during the reductive quenching of the acridinium **5** (Fig. 3c). Hence, **11** can react with either radicals **12** or **13**, leading to compound **14** or **10**, respectively. It is worth noting that all these species (**10**, **14** and **phoenix1**) are reversibly generated under light irradiation (Fig. 4).

The dimerization of **11** leading to **phoenix1** regeneration has a ΔG of −21.1 kcal mol^{-1}. Although the reaction with **12** or **13** is even more favourable (ΔG of −23.4 kcal mol^{-1} and −30.3 kcal mol^{-1} for the formation of **14** and **10**, respectively), we never observed the formation of **14**, and we detected **10** only in the initial reaction with **5** at the 1-mmol scale (Fig. 2 and vide infra). We attribute the observed preferred selectivity to the preferential reactivity of radicals **12** and **13** to irreversibly yield **3** (ΔG of −43.8 kcal mol^{-1}), which is not photoactive above 400 nm and thus acts as the primary molecular sink.

To better investigate the role of **10** in the catalytic manifold, we performed ^{19}F-NMR kinetic analysis on the crude reaction mixture with the fluorinated silane **15** (Fig. 5a and 'Kinetic Analysis' in Supplementary Information). Interestingly, we observed that the reaction initially mainly delivers **18**, the homocoupling dimer of the starting silane **15**, while its concentration is virtually constant until the end of the reaction (33% NMR yield). With a similar slope, product **17** and benzylated acridine **16** form until 3 h (at 20% and 14% NMR yields, respectively). After 3 h, while **16** rapidly decreases, **17** increases at a greater speed reaching a 55% NMR yield. At the end of the process, no trace of **16** is detected with complete recovery of the original **phoenix1**. These experiments indicate that **16** has a significant role in the reaction: the accumulation of **16** culminates in an accelerated productive regime for the formation of **17**. We can assume that between 3 h and 4 h, two mechanistic paths are active and incrementally lead to the formation of **17**.

Taking into consideration these findings, we propose a comprehensive reaction manifold involving the catalytic activity of benzylated acridine **10** (Fig. 5b and 'Scrambling Experiments', 'Kinetic Analysis' and 'Photophysical Studies' in Supplementary Information). It is worth noting that, here, **10** also acts as a molecular shuttle, being rapidly generated from radicals **11** and **13** ($k = 1.7 \times 10^9$ M^{-1} s^{-1}; Supplementary Fig. 77), thus preventing the unwanted dimerization of **13**. This potentially improves the overall selectivity of the process without the need for any radical sorting reagents[32]. To further support this mechanism, we performed additional photophysical studies. Upon light irradiation, **10** is excited, and its S_1 state (lifetime, $\tau = 2.8$ ns) is promptly quenched dynamically ($k = 4.9 \times 10^9$ M^{-1} s^{-1}) by **1**, leading to the formation of benzyl radical **13**, which reacts with **12**, yielding the coupling product **3**. At the same time, **5** is regenerated and promotes the photo-oxidation of **2** (for details, see 'Photophysical Studies' in Supplementary Information). In light of all the experiments performed and the measured rate constants, we can conclude that two intimately interconnected mechanisms are responsible for the production of **3**, as well as the observed selectivity: one involves the direct regeneration of **phoenix1** from two acridine radical **11** (Fig. 3e), the second yet productive pathway involves first the in situ generation of **10** from **11** followed by the regeneration of **5** and ultimately converging into the regeneration of **phoenix1**.

https://doi.org/10.1038/s41929-026-01593-w

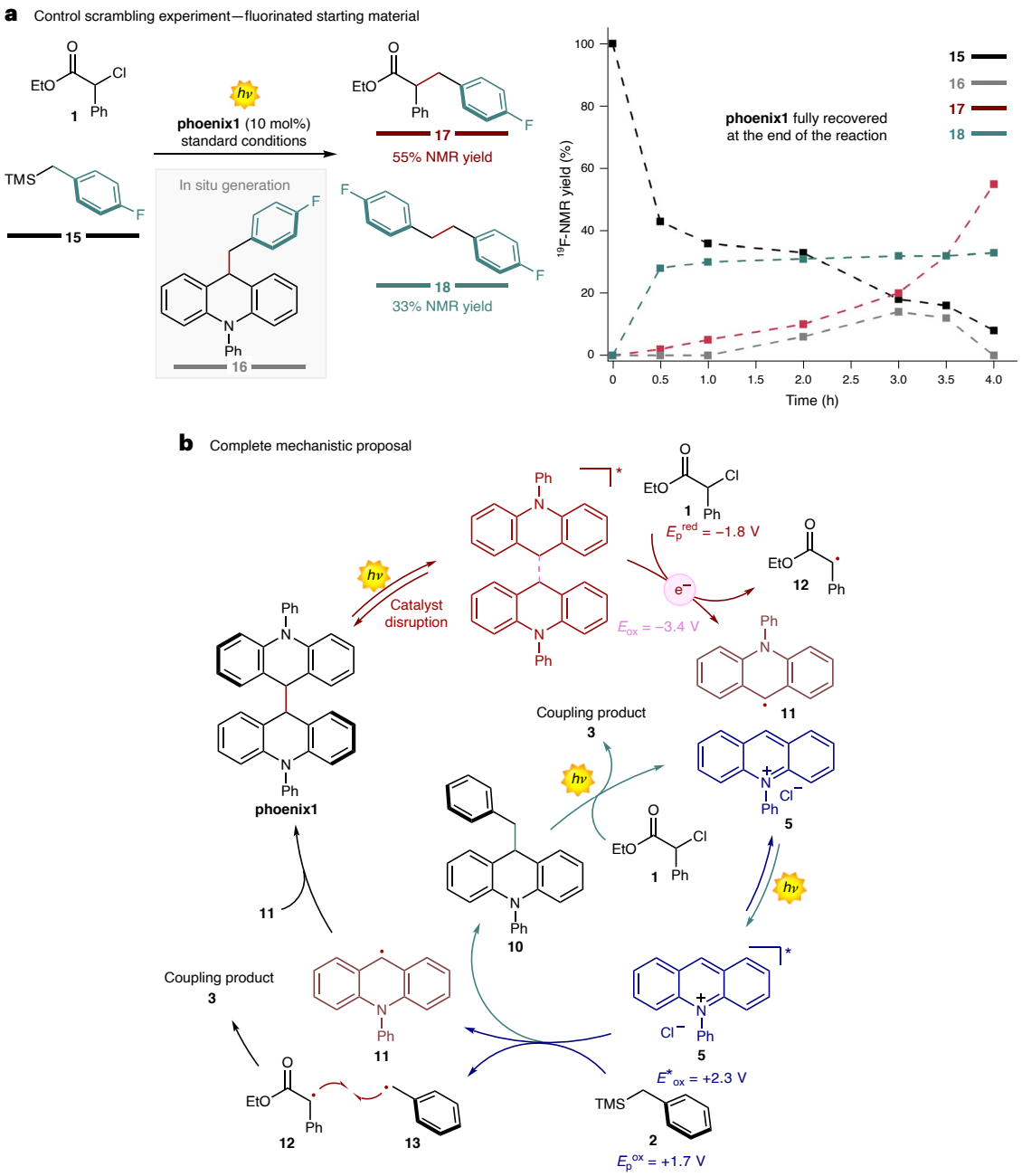

Fig. 5 | Overall mechanistic picture. a, Scrambling experiment and kinetic analysis performed under standard conditions (see 'Scrambling Experiments' and 'Kinetic Analysis' in Supplementary Information). **b**, Complete mechanistic scenario.

Synthetic applications of bimodal multiphoton catalysis

After elucidating the dynamic nature of the catalytic machinery, we evaluated its generality and functional group tolerance (Fig. 6). We initially assessed the tolerance of diverse aryl and heteroaryl groups at the α-position of the ester (**19**–**24**). Later, we focus our interest on products bearing all-carbon quaternary centres—difficult to access under thermal means. Pleasingly, 2,2-diphenyl α-chloro esters were the most effective substrates with yields up to 78% for **22**. The reaction was also tolerant of diverse aromatic and heterocyclic trimethylsilyl (TMS) derivatives, leading to **25**–**33** in yields up to 63%. Particularly significant is product **25**; this compound bears an all-carbon quaternary centre together with a pyridine ring and requires a redox power as high as 3.9 V, corresponding to 317 nm. Under dynamic photocatalysis, however, it is possible to access it using visible light. Allylation reactions are also possible under the developed conditions (**28**). Remarkably, more complex chiral α-amino acids with free NH groups were also converted into the corresponding alkylated products (**29**–**31**) with aryl as well as heterocyclic systems with yields up to 63%. Similarly, nitriles and sulphones (see 'Additional Products' in Supplementary Information) were competent substrates, although delivering the corresponding products with inferior results. It is worth noting that several of these products, bearing all-carbon quaternary centres (**21**–**28**), as well as free NH groups or stereocentres (**29**–**31**), are not accessible via classical enolate-based procedures[33].

We next turned our attention to substrates with different chemical characteristics (Fig. 6). Interestingly, bromodifluoromethyl compounds can be effectively transformed into the corresponding gem-difluoro coupling derivatives (up to 47% yield). It is worth noting that the only method to synthesize such compounds required the use of transition metal catalysis in the presence of bis-pyridine

https://doi.org/10.1038/s41929-026-01593-w

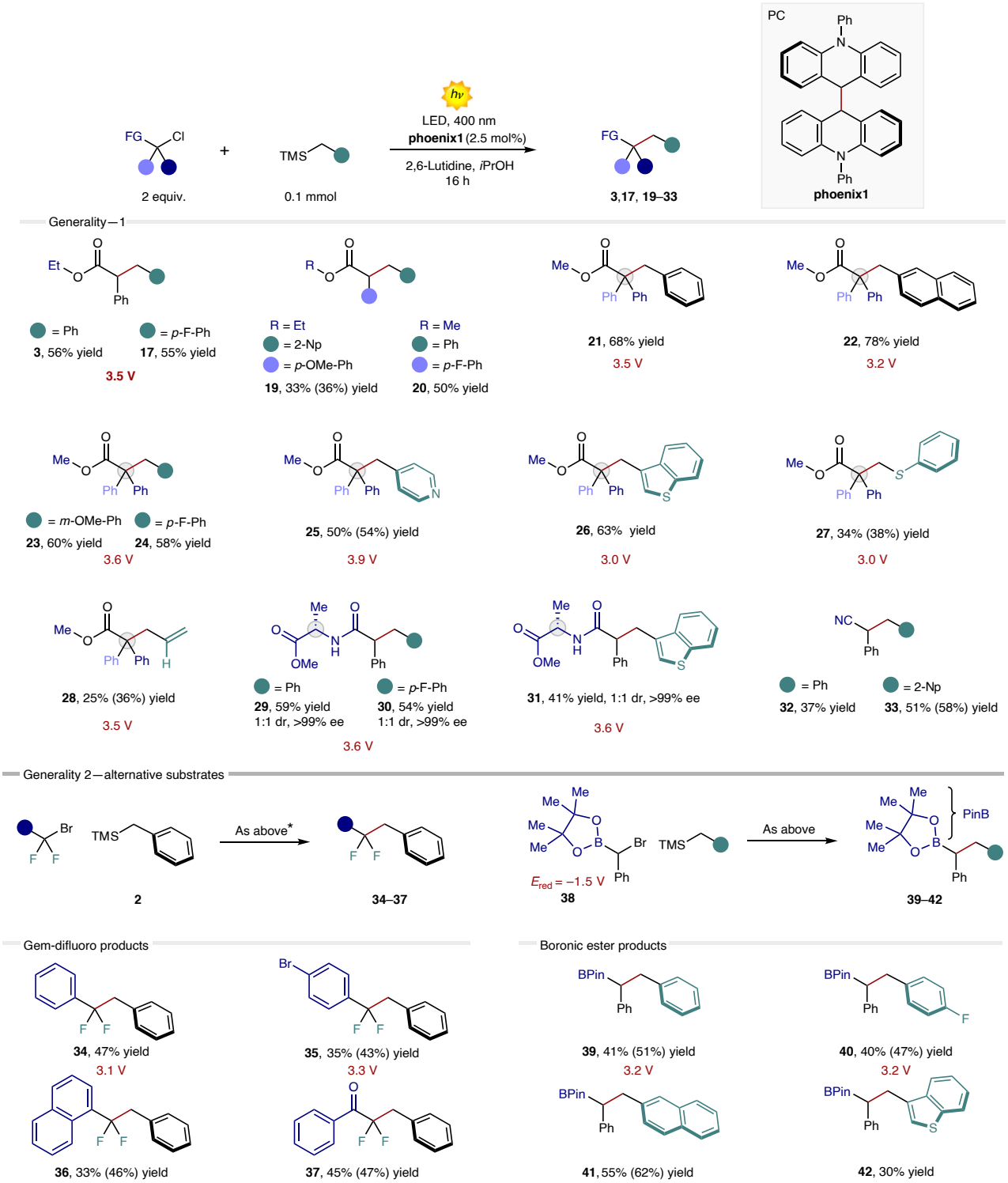

Fig. 6 | Generality of the developed regenerative photocatalytic manifold. Reaction conditions: α-chloro derivative (0.2 mmol), silane derivative (0.1 mmol), **phoenix1** (2.5 mol%), 2,6-lutidine (0.3 mmol) in *i*PrOH [0.1 M], irradiated with a 50-W Kessil lamp (400 nm, 3 cm distance) under a nitrogen atmosphere at 30 °C. The reported yields refer to the average of two independent reactions. Yields in parentheses refer to the NMR yield of the crude mixture measured with 1,3,5-trimethoxybenzene as an internal standard. Unless otherwise noted, all the potential values refer to V versus the SCE. FG, functional group; 2-Np, 2-naphthyl.

ligands at 80 °C over 24 h (ref. 34). Here dynamic photocatalysis offers an alternative milder and more sustainable option. To further challenge the developed dynamic photocatalytic process, we performed reactions between the α-bromo boronic ester **38** ($E_{red} \leq -1.5$ V versus the SCE; Supplementary Figs. 42 and 43) and different silane reagents. The corresponding products **39**–**42** were obtained in yields up to 55%. Remarkably, we used this approach to prepare boronic ester derivatives bearing heterocyclic functionalities, which are elusive to synthesize via classical metal-based borylation strategies[35,36].

Conclusions

In summary, we have described an unconventional catalytic manifold that enables thermodynamically challenging reduction and oxidation within the same reaction. Combined femto- and nanosecond transient absorption measurements, EPR spectroscopy, spectroelectrochemistry and DFT calculations provided detailed insight into the operative reaction manifolds, which involve a rare photoionization event. While the generated solvated electrons, with an $E_{red} < -3.4$ V versus the SCE, activate inert C–Cl, C–Br, C–B and C–O bonds, the acridinium undergoes excitation, delivering a potent excited-state oxidant ($E^*_{red} = +2.3$ V versus the SCE) that can oxidize silanes, BF_3 salts or boronic esters. These reduced and oxidized species undergo radical combination to deliver the corresponding coupling products (52 examples, up to 78% yield). Importantly, the original photocatalytic system is restored by another radical recombination. The selectivity of the process is governed by the reversible nature of the in situ-formed radical-coupling products, as well as by the activity of a transiently generated acridine catalytic species, thus avoiding the need for any radical sorting agents. Interestingly, this catalytic platform merges two distinct and thermodynamically opposed redox quenching cycles, accessing a redox window as broad as 5.7 V. Here the intrinsic fragility of the PC scaffold becomes its strength, allowing selective C–C bond breaking and the resulting dual reaction manifold.

Methods

General procedure for dynamic photochemical process

A 4-ml glass vial was charged with the corresponding α-halogenated derivative (0.2 mmol, 2 equiv.), **phoenix1** (0.0025 mmol, 2.5 mol%), 2,6-lutidine (0.3 mmol, 3 equiv.) and 2-propanol (*i*PrOH, 1 ml, 0.1 M). The reaction mixture was degassed by sparging N_2 for 2 min, before adding the appropriate silane derivative (0.1 mmol, 1 equiv.; if not volatile, it can be added before degassing the reaction mixture). The vessel was sealed with parafilm and placed into a photoreactor (irradiation wavelenght $\lambda = 400$ nm, 50 W, 3 cm distance). The temperature was kept at room temperature, typically 23–26 °C, by using a fan. Stirring was maintained for 16 h; then the irradiation was stopped. The volatiles were removed under reduced pressure; the residue was dissolved in $CDCl_3$, and the yield of the desired product was determined by ^{1}H-NMR and/or ^{19}F-NMR spectroscopy using an internal standard. After removing the solvent in vacuo, the crude product was purified by automated flash column chromatography (hexane/ethyl acetate), or the residue was filtered over a silica pad eluting with hexane/ethyl acetate 8:2 to 1:1 *v*/*v* and further purified by preparative HPLC on a C18 reversed-phase column using acetonitrile (A) and water (B) as mobile phases at a flow rate of 17 ml min^{-1}. The following gradient was applied: 5 min at 5% B, then a linear increase from 5% to 100% B over 60 min and 10 min at 100% B.

Data availability

Details of the materials and methods, experimental procedures, mechanistic studies, characterization data and NMR spectra are available in Supplementary Information. The atomic coordinates of the optimized models for all the computational studies are available as a separate public file. Crystallographic data are available from the Cambridge Crystallographic Data Centre with the following code: **phoenix1** (CCDC 2381856).

References

1. Romero, N. A. & Nicewicz, D. A. Organic photoredox catalysis. *Chem. Rev.* **116**, 10075–10166 (2016).
2. Shaw, M. H., Twilton, J. & MacMillan, D. W. C. Photoredox catalysis in organic chemistry. *J. Org. Chem.* **81**, 6898–6926 (2016).
3. Vega-Peñaloza, A., Mateos, J., Companyó, X., Escudero-Casao, M. & Dell'Amico, L. A rational approach to organo-photocatalysis: novel designs and structure–property relationships. *Angew. Chem. Int. Ed.* **60**, 1082–1097 (2021).
4. Arias-Rotondo, D. M. & McCusker, J. K. The photophysics of photoredox catalysis: a roadmap for catalyst design. *Chem. Soc. Rev.* **45**, 5803–5820 (2016).
5. Balzani, V., Ceroni, P., & Juris, A. *Photochemistry and Photophysics: Concepts, Research, Applications* (Wiley, 2014).
6. Dutta, S., Erchinger, J. E., Strieth-Kalthoff, F., Kleinmans, R. & Glorius, F. Energy transfer photocatalysis: exciting modes of reactivity. *Chem. Soc. Rev.* **53**, 1068–1089 (2024).
7. Twilton, J. et al. The merger of transition metal and photocatalysis. *Nat. Rev. Chem.* **1**, 0052 (2017).
8. Tucker, J. W. & Stephenson, C. R. J. Shining light on photoredox catalysis: theory and synthetic applications. *J. Org. Chem.* **77**, 1617–1622 (2012).
9. Glaser, F., Kerzig, C. & Wenger, O. S. Multi-photon excitation in photoredox catalysis: concepts, applications, methods. *Angew. Chem. Int. Ed.* **59**, 10266–10284 (2020).
10. Mateos, J. et al. Naphthochromenones: organic bimodal photocatalysts engaging in both oxidative and reductive quenching processes. *Angew. Chem. Int. Ed.* **59**, 1302–1312 (2020).
11. Tlili, A. & Lakhdar, S. Acridinium salts and cyanoarenes as powerful photocatalysts: opportunities in organic synthesis. *Angew. Chem. Int. Ed.* **60**, 19526–19549 (2021).
12. Shee, M. et al. Modulating p–π conjugation with hybridized local and charge-transfer excited-state manifolds: toward bimodal photocatalysts for efficient energy and electron transfer catalysis. *ACS Catal.* **15**, 18204–18217 (2025).
13. Murray, P. R. D. et al. Photochemical and electrochemical applications of proton-coupled electron transfer in organic synthesis. *Chem. Rev.* **122**, 2017–2291 (2022).
14. Bortolato, T. et al. The rational design of reducing organophotoredox catalysts unlocks proton-coupled electron-transfer and atom transfer radical polymerization mechanisms. *J. Am. Chem. Soc.* **145**, 1835–1846 (2023).
15. Agarwal, R. G. et al. Free energies of proton-coupled electron transfer reagents and their applications. *Chem. Rev.* **122**, 1–49 (2022).
16. Ghosh, I., Ghosh, T., Bardagi, J. I. & Konig, B. Reduction of aryl halides by consecutive visible light-induced electron transfer processes. *Science* **346**, 725–728 (2014).
17. Cowper, N. G. W., Chernowsky, C. P., Williams, O. P. & Wickens, Z. K. Potent reductants via electron-primed photoredox catalysis: unlocking aryl chlorides for radical coupling. *J. Am. Chem. Soc.* **142**, 2093–2099 (2020).
18. Chernowsky, C. P., Chmiel, A. F. & Wickens, Z. K. Electrochemical activation of diverse conventional photoredox catalysts induces potent photoreductant activity. *Angew. Chem. Int. Ed.* **60**, 21418–21425 (2021).
19. Huang, H., Steiniger, K. A. & Lambert, T. H. Electrophotocatalysis: combining light and electricity to catalyze reactions. *J. Am. Chem. Soc.* **144**, 12567–12583 (2022).
20. Andrieux, C. P., Le Gorande, A. & Saveant, J. M. Electron transfer and bond breaking. Examples of passage from a sequential to a concerted mechanism in the electrochemical reductive cleavage of arylmethyl halides. *J. Am. Chem. Soc.* **114**, 6892–6904 (1992).
21. Isse, A. A., Lin, C. Y., Coote, M. L. & Gennaro, A. Estimation of standard reduction potentials of halogen atoms and alkyl halides. *J. Phys. Chem. B* **115**, 678–684 (2011).
22. Jacobi, D., Abraham, W., Pischel, U., Stößer, R. & Schnabel, W. Reduction of aryl tropylium ions by thermal hydride transfer or by photochemical reactions. *J. Photochem. Photobiol. A* **128**, 75–83 (1999).
23. Chase, W. J. & Hunt, J. W. Solvation time of the electron in polar liquids. Water and alcohols. *J. Phys. Chem.* **79**, 2835–2845 (1975).

24. Hiratsuka, H., Sekiguchi, K., Hatano, Y. & Tanizaki, Y. Polarized absorption and ESR spectra of acridine C-radical. *Chem. Phys. Lett.* **55**, 358–360 (1978).
25. Benniston, A. C., Harriman, A., Li, P., Rostron, J. P. & Verhoeven, J. W. Illumination of the 9-mesityl-10-methylacridinium ion does not give a long-lived photoredox state. *Chem. Commun.* **7**, 2701 (2005).
26. Madden, K. P. & Taniguchi, H. The role of the DMPO-hydrated electron spin adduct in DMPO-OH spin trapping. *Free Radic. Biol. Med.* **30**, 1374–1380 (2001).
27. Novelli, F. et al. The birth and evolution of solvated electrons in the water. *Proc. Natl Acad. Sci. USA* **120**, e2216480120 (2023).
28. Shaikh, A. C. et al. Solvated electrons! The missing link in highly reducing photocatalysis. Preprint at *ChemRxiv* https://doi.org/10.26434/chemrxiv-2022-6qpb8 (2022).
29. Singh, P., Lal, N. & Shaikh, A. C. Solvated electrons: dynamic reductant in visible light photoredox catalysis. *Adv. Synth. Catal.* **366**, 1906–1921 (2024).
30. Villa, M. et al. Organic super-reducing photocatalysts generate solvated electrons via two consecutive photon induced processes. *Chem. Sci.* https://doi.org/10.1039/d4sc04518a (2024).
31. Panetti, G. B. et al. Photodriven ammonia synthesis from manganese nitrides: photophysics and mechanistic investigations. *J. Am. Chem. Soc.* **146**, 27610–27621 (2024).
32. Cai, Q., McWhinnie, I. M., Dow, N. W., Chan, A. Y. & MacMillan, D. W. C. Engaging alkenes in metallaphotoredox: a triple catalytic, radical sorting approach to olefin-alcohol cross-coupling. *J. Am. Chem. Soc.* **146**, 12300–12309 (2024).
33. Wright, T. B. & Evans, P. A. Catalytic enantioselective alkylation of prochiral enolates. *Chem. Rev.* **121**, 9196–9242 (2021).
34. Xiao, Y., Min, Q., Xu, C., Wang, R. & Zhang, X. Nickel-catalyzed difluoroalkylation of (hetero)arylborons with unactivated 1-bromo-1,1-difluoroalkanes. *Angew. Chem. Int. Ed.* **55**, 5837–5841 (2016).
35. Wang, B. J. & Groziak, M. P. *Advances in Heterocyclic Chemistry* (Elsevier, 2016).
36. Ahmed, A., Mushtaq, I. & Chinnam, S. Suzuki–Miyaura cross-couplings for alkyl boron reagent: recent developments—a review. *Futur. J. Pharm. Sci.* **9**, 67 (2023).

Acknowledgements

We gratefully acknowledge the technical support units at the Department of Chemical Sciences (DiSC) of the University of Padova, in particular, I. Fortunati, S. Pressi and S. Mercanzin.

Author contributions

L.D. designed the project and devised the experiments with C.R. and G. Barison. C.R., G. Barison and N.M. carried out the reactions and isolated and characterized the products with A.M. L.D., C.R. and G. Barison rationalized the experimental results. M.N. and F.D. performed the spectroscopic investigations using transient absorption spectroscopy at the ns timescale. V.B. and E.C. performed the spectroscopic investigations using transient absorption spectroscopy at the ps timescale. P.C., A.S., G. Bistoni and S.L. performed the DFT calculations. G. Bistoni and S.L. performed the computational analysis on the reaction profiles. S.B., S.V. and A.S. performed the spectroelectrochemical experiments with C.R. and G. Barison M.B. performed the EPR measurements with G. Barison. G.P. performed the X-ray analysis. S.V. performed the CV and the SEC with G. Barison and C.R. L.D. wrote the paper with contributions from all the authors. L.D. directed and supervised the work and secured funding.

Funding

This work was supported by Ministero dell'Università (MUR) PRIN 2020927WY3 (M.N. and L.D.), PRIN2022PNRR23_01 (L.D.) and European Research Council (ERC) Starting Grant 2021 SYNPHOCAT 101040025 (L.D., C.R. and G.B.). Open access funding provided by Università degli Studi di Padova within the CRUI-CARE Agreement.

Competing interests

The authors declare no competing interests.

Additional information

Supplementary information The online version contains supplementary material available at https://doi.org/10.1038/s41929-026-01593-w.

Correspondence and requests for materials should be addressed to Luca Dell'Amico.

Peer review information *Nature Catalysis* thanks the anonymous reviewers for their contribution to the peer review of this work. Peer reviewer reports are available.

Reprints and permissions information is available at www.nature.com/reprints.

Publisher's note Springer Nature remains neutral with regard to jurisdictional claims in published maps and institutional affiliations.

Open Access This article is licensed under a Creative Commons Attribution 4.0 International License, which permits use, sharing, adaptation, distribution and reproduction in any medium or format, as long as you give appropriate credit to the original author(s) and the source, provide a link to the Creative Commons licence, and indicate if changes were made. The images or other third party material in this article are included in the article's Creative Commons licence, unless indicated otherwise in a credit line to the material. If material is not included in the article's Creative Commons licence and your intended use is not permitted by statutory regulation or exceeds the permitted use, you will need to obtain permission directly from the copyright holder. To view a copy of this licence, visit http://creativecommons.org/licenses/by/4.0/.

© The Author(s) 2026